

# Pressure effects on the electronic structure and magnetic properties of infinite-layer nickelates

Shekhar Sharma,<sup>1,\*</sup> Myung-Chul Jung,<sup>2</sup> Harrison LaBollita,<sup>1</sup> and Antia S. Botana<sup>1</sup>

<sup>1</sup>*Department of Physics, Arizona State University, Tempe, AZ 85287, USA*

<sup>2</sup>*Department of Physics Education, Chosun University,  
30 Chosundae3gil, Dong-gu, Gwangju, South Korea, 61452*

(Dated: March 13, 2024)

Motivated by the discovery of superconductivity in infinite-layer nickelates  $\text{RNiO}_2$  ( $R$ = rare-earth), and the subsequent enhancement of their  $T_c$  with pressure, we investigate the evolution of the electronic structure and magnetic properties of this family of materials via first-principles calculations employing hydrostatic and chemical pressure as tuning knobs. Overall, our analysis shows that pressure tends to increase the  $R$ - $5d$  self-doping effect, as well as the  $\text{Ni-}d_{x^2-y^2}$  bandwidth, the  $e_g$  energy splitting, the charge transfer energy, and the superexchange ( $J$ ). Using the energy scale of  $J$  as a predictor of superconducting tendencies, we anticipate that pressure can indeed be a feasible means to further increase the  $T_c$  in this family of materials.

## I. INTRODUCTION

The discovery of high- $T_c$  superconductivity (HTS) in the cuprates [1] triggered attempts to find analog superconducting materials aimed at identifying the requisite ingredients for HTS [2]. In this context, nickelates have been intensively investigated given the proximity of Ni to Cu in the periodic table [3, 4]. Nickelate superconductivity was first realized in 2019 in hole-doped infinite-layer  $\text{Nd}_{1-x}\text{Sr}_x\text{NiO}_2$  thin films with  $T_c \sim 15$  K [5]. This initial discovery immediately attracted extensive theoretical and experimental efforts [6–36] that gave rise to the subsequent discovery of superconductivity in hole-doped infinite-layer nickelates with other rare-earth cations [10, 37, 38], in a quintuple-layer nickelate ( $\text{Nd}_6\text{Ni}_5\text{O}_{12}$ ) without chemical doping [39], and most recently in the parent Ruddlesden-Popper bilayer [40–42] and trilayer [43–45] nickelates upon applying hydrostatic pressure. Focusing on the infinite-layer nickelates, these materials exhibit striking similarities to the cuprates. Structurally, both materials host two-dimensional square planes of transition-metal (TM) and O atoms [46, 47]. In terms of filling, both are in proximity to a  $3d^9$  electronic configuration with superconductivity arising near 20% hole doping. The  $e_g$  splitting – correlated with  $T_c$  in the cuprates, with a larger value giving rise to a higher  $T_c$  due to reduced mixing of these orbitals [48, 49] – is also similar in infinite-layer nickelates [50]. Theoretical and experimental work suggests an unconventional ( $d$ -wave) pairing mechanism for superconductivity in these nickelates, akin to the cuprates [11, 32, 51, 52]. Further, a recent analysis of pressure effects on hole-doped  $\text{PrNiO}_2$  thin films [53] has revealed a substantial increase in  $T_c$  (from 18 K to 31 K) under 12 GPa, following the pressure-enhanced  $T_c$  trends of the cuprates [54]. In spite of these similarities, there are, however, some important differences between infinite-layer nickelates and cuprates that have been intensively studied

[3, 50]. The cuprates are antiferromagnetic charge-transfer insulators close to the  $3d^9$  limit that portray a single band of  $d_{x^2-y^2}$  character near the Fermi level, and are known to exhibit a large degree of O- $p$  and Cu- $d$  hybridization [2]. For infinite-layer nickelates, the lower degree of hybridization between the Ni- $d$  and O- $p$  states as well as the presence of additional ‘spectator’ or ‘self-doping’ bands of rare-earth (R)- $d$  character at the Fermi level are distinguishing factors [55]. These rare-earth electron pockets that self-dope the Ni- $d_{x^2-y^2}$  band preempt the possibility of an antiferromagnetic insulating state in the parent phase, even though the presence of strong antiferromagnetic correlations has recently been reported via resonant inelastic x-ray scattering (RIXS) experiments [56].

In light of the experimental enhancement of  $T_c$  in infinite-layer nickelates with pressure (together with the recent explosion of work on superconductivity in pressurized Ruddlesden-Popper nickelates), here, we study the effects of hydrostatic pressure on the electronic structure and magnetic response of infinite-layer nickelates. Using first-principles calculations, we report the systematic evolution of the dominant similarities and differences between infinite-layer ( $\text{RNiO}_2$ ) nickelates and cuprates with pressure. Further, we correlate the changes arising from hydrostatic pressure with changes in chemical pressure, by exploring different rare-earth ions. We find that both hydrostatic and chemical pressure can be used as a “knob” to tune the electronic and magnetic response in infinite-layer nickelates to ultimately enhance their  $T_c$ .

## II. COMPUTATIONAL DETAILS

The  $\text{RNiO}_2$  ( $R$  = rare-earth) nickelates are the infinite layer ( $n = \infty$ ) members of the reduced Ruddlesden-Popper (RP) series  $\text{R}_{n+1}\text{Ni}_n\text{O}_{2n+2}$ . Their crystal structure has been resolved in the  $P4/mmm$  space group at ambient pressure [46, 47] (see Fig. 1(a)). We have performed density-functional theory (DFT)-based calculations for the La-based infinite-layer nickelate  $\text{LaNiO}_2$

\* sshar246@asu.edu

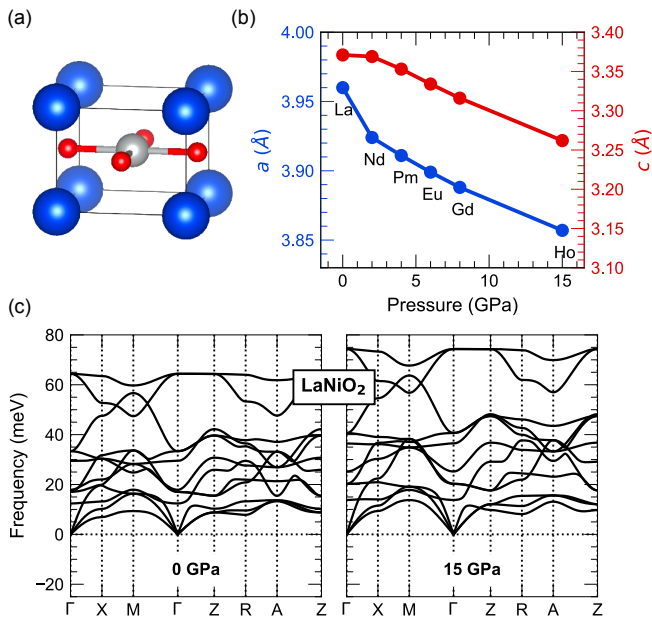


FIG. 1. Crystal structure and lattice stability of pressurized infinite-layer RNiO<sub>2</sub>. (a) Crystal structure of RNiO<sub>2</sub> nickelates ( $P4/mmm$ ) where blue, grey, and red spheres denote R, Ni, and O atoms, respectively. (b) DFT-optimized lattice constants for pressurized LaNiO<sub>2</sub> with corresponding rare-earth cations matched to the in-plane lattice constant of LaNiO<sub>2</sub> at a certain pressure. (c) Phonon dispersions for LaNiO<sub>2</sub> at ambient pressure (left) and 15 GPa (right).

under pressures up to 15 GPa, relevant to the experiments in Ref. [53]. For all pressures, we conducted structural relaxations using the Vienna *ab-initio* Simulation Package (VASP), optimizing both the lattice parameters and the internal coordinates [57, 58]. The generalized gradient approximation (GGA) as implemented in the Perdew-Burke-Ernzerhof (PBE) functional was used as the exchange-correlation functional [59]. An energy cutoff of 500 eV and a  $k$ -mesh of  $20 \times 20 \times 20$  were adopted with a force convergence criterion of  $10^{-2}$  meV/Å. The same structural optimization procedure was used for RNiO<sub>2</sub> (R = Nd, Pm, Eu, Gd, Ho). The lattice dynamics of RNiO<sub>2</sub> were further investigated using the frozen phonon method with  $2 \times 2 \times 2$  supercells as implemented in PHONOPY [60] interfaced with VASP.

Subsequently, for each optimized structure, we analyzed the evolution of the non-magnetic electronic structure with pressure using the full-potential, all-electron code WIEN2K [61]. In these calculations, we also employed PBE-GGA as the exchange-correlation functional. We used  $R_{\text{MT}}K_{\text{max}} = 7$  and a  $k$ -grid of  $19 \times 19 \times 22$  for the Brillouin zone sampling. Electronic structure calculations for different rare-earth ions (R = Nd, Pm, Eu, Gd, Ho) were performed using the same computational parameters within the open-core approximation for the R-4*f* electrons.

To gain further insight into the electronic structure and to obtain quantitative trends with pressure, we

downfolded the Kohn-Sham DFT band structures onto maximally localized Wannier functions (MLWFs) to extract on-site energies and relevant hopping integrals as implemented in WANNIER90 [62] interfaced with WIEN2WANNIER [63]. We chose a  $d-p$  basis, where all the Ni-3*d* and O-2*p* orbitals were taken in the initial projections.

The magnetic tendencies of RNiO<sub>2</sub> under the application of hydrostatic pressure (for R = La at  $P = 0-15$  GPa) as well as for chemical pressure (R = Nd, Pm, Eu, Gd, Ho) were explored via GGA+*U* (as implemented in VASP with the R-4*f* states in the pseudopotential core) calculations employing the fully-localized limit (FLL) as the double counting correction [64]. Two different values for the on-site Coulomb repulsion *U* of 2 eV and 7 eV were applied to the Ni-3*d* states to understand the energetic dependence with *U*. We considered two different antiferromagnetic (AFM) configurations that have been shown to be the lower energy ones in RNiO<sub>2</sub> in previous DFT work [65, 66]: (1) AFM-G where antiferromagnetic planes are coupled antiferromagnetically out-of-plane and (2) AFM-C where antiferromagnetic planes are coupled ferromagnetically out-of-plane.

### III. RESULTS

#### A. Crystal structure and lattice dynamics

We start by describing the changes in the crystal structure of LaNiO<sub>2</sub> with hydrostatic pressure. The corresponding optimized lattice parameters are shown in Fig 1(b). As expected, both the in-plane and out-of-plane lattice constants get reduced (by approximately a 3%) from ambient pressure to 15 GPa. We find that up to the highest pressure we studied the space group remains as  $P4/mmm$  (even allowing for symmetry reduction in the structural relaxations) as reflected in the calculated phonon dispersions shown in Fig. 1(c) where no imaginary modes can be observed in the spectrum for LaNiO<sub>2</sub> all the way up to 15 GPa.

To perform a meaningful comparison between the effects of hydrostatic and chemical pressure, we make an approximate ‘one-to-one’ mapping between the in-plane lattice constant (*a*) obtained for a certain rare-earth ion after a full structural relaxation and the corresponding pressure value applied to LaNiO<sub>2</sub>. We focus on matching the in-plane lattice constant as we determined in previous work that this is the most relevant tuning knob for the electronic structure across the rare-earth series for RNiO<sub>2</sub> [65]. In this manner, we obtain a correspondence between NdNiO<sub>2</sub>, PmNiO<sub>2</sub>, EuNiO<sub>2</sub>, GdNiO<sub>2</sub>, and HoNiO<sub>2</sub> and pressures of 2, 4, 6, 8, and 15 GPa applied to LaNiO<sub>2</sub>, respectively (see Fig. 1(b)). The accompanying out-of-plane lattice constant for each rare-earth is slightly smaller than that obtained for the corresponding in-plane lattice-matched pressure (the optimization yields a systematic reduction of the out-of-plane lattice constant *c* by

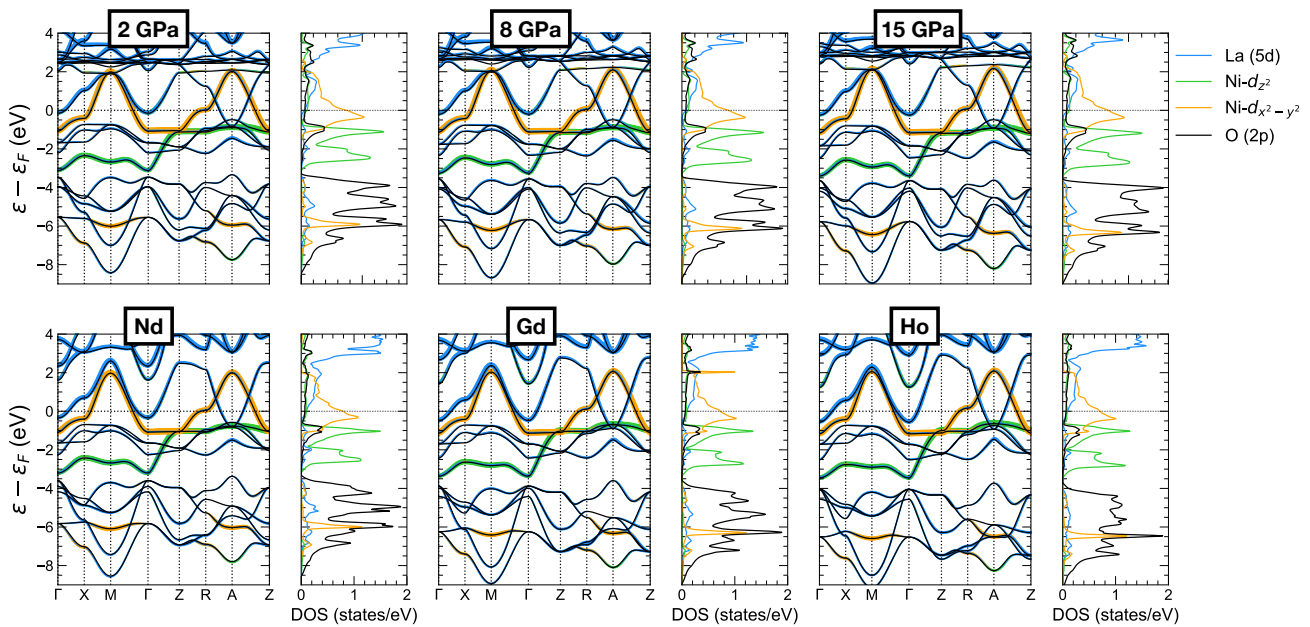


FIG. 2. Comparison between the non-magnetic electronic structure with hydrostatic (top) and chemical (bottom) pressure. Top row: Band structure along high-symmetry lines and atom-, orbital-resolved density of states (DOS) for  $\text{LaNiO}_2$  at 2 GPa, 8 GPa, and 15 GPa (from left to right). The orbital character of the bands is denoted for  $\text{Ni-}d_{x^2-y^2}$  (orange),  $\text{Ni-}d_{z^2}$  (green), and  $\text{R-}d$  (blue). Bottom row: Equivalent plots to those of the top row for  $\text{RNiO}_2$  with  $\text{R} = \text{Nd, Gd, and Ho}$  (from left to right).

about 10% across the lanthanide series as can be seen in Table I in Appendix A). We note that it has been shown previously [67, 68] that below a critical rare-earth ionic radius, the  $P4/mmm$  crystal structure becomes unstable in  $\text{RNiO}_2$  with a lattice instability at A transforming the structure from  $P4/mmm$  to  $I4/mcm$  (see Fig. 6 in Appendix B). However, as mentioned above, for  $\text{LaNiO}_2$  the  $P4/mmm$  structure is stable for all the pressures considered here. Therefore, to perform a one-to-one comparison between chemical and hydrostatic pressure in subsequent sections, we will restrict ourselves to analyzing all  $\text{RNiO}_2$  compounds in a  $P4/mmm$  space group.

### B. Electronic structure with pressure

We will start by revisiting the basic features of the nonmagnetic electronic structure of  $\text{LaNiO}_2$  at ambient pressure. As shown early on [3, 50], three bands near the Fermi level contribute to the low-energy physics of this material. First, a two-dimensional  $\text{Ni-}3d_{x^2-y^2}$ -derived band crosses the Fermi level, reminiscent of the cuprates. But, as mentioned above, the infinite-layer nickelates host additional  $\text{La-}5d$  ‘spectator’ bands which self-dope the  $\text{Ni-}3d_{x^2-y^2}$  orbital. These  $\text{La-}5d$  bands generate two electron pockets: one at  $\Gamma$  with mostly  $\text{La-}d_{z^2}$  character and one at A with mostly  $\text{La-}d_{xy}$  character. Importantly, the  $5d$  bands have a three-dimensional dispersion giving rise to strong out-of-plane couplings [69, 70]. The self-doping effect (that corresponds to around 5% holes in the  $\text{Ni-}d_{x^2-y^2}$  orbital) causes a shift away from nominally

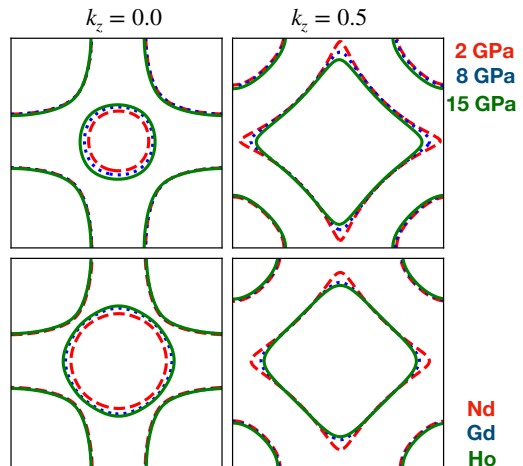


FIG. 3. Evolution of Fermi surface under hydrostatic (top) and chemical (bottom) pressure in the  $k_z = 0$  (left) and  $k_z = 1/2$  planes (right).

half-filling. Therefore, the infinite-layer nickelates can be thought of as underdoped cuprates even at stoichiometry (i.e. nominal  $d^9$  filling). Further, when compared to cuprates, the  $\text{O-}2p$  bands in infinite-layer nickelates are much lower in energy relative to the  $\text{Ni-}3d$  bands, giving rise to a  $\sim 4.3$  eV charge-transfer energy, which is much larger than typical cuprate values  $\sim 1 - 2$  eV [71]. In this context, an important question in infinite-layer nickelates has been their placement on the charge transfer-Mott continuum defined by Zaanen, Sawatzky

and Allen [72]. A recent RIXS study [73] suggests that the reduced nickelates are intermediate between the charge transfer and Mott limits.

We now turn to the electronic structure of  $\text{LaNiO}_2$  under the influence of hydrostatic and chemical pressure. Fig. 2 shows the band structure evolution – with the relevant orbital characters highlighted – as well as the corresponding atom and orbital-projected density of states (DOS) up to 15 GPa for  $\text{LaNiO}_2$  as well as for  $\text{RNiO}_2$  with  $R = \text{Nd}$  (matching 2 GPa),  $R = \text{Pm}$  (matching 8 GPa) and  $R = \text{Ho}$  (matching 15 GPa) (further pressures and  $R$  ions are shown in Fig. 7 in Appendix C). We focus first on the evolution with hydrostatic pressure of the  $\text{Ni-}d_{x^2-y^2}$  band that crosses the Fermi level in  $\text{LaNiO}_2$ : its bandwidth increases monotonically by about a 5% with pressures up to 15 GPa. This is expected considering the trend in lattice constants shown in the previous section: a reduction in the in-plane constants leads to increased orbital overlap and, as a consequence, in the hybridization and bandwidth. A similar increase in bandwidth is observed when reducing the size of the rare-earth ion from La to Ho.

The electron pockets associated with the rare-earth  $5d$  bands that cross the Fermi level can be seen to increase in size with pressure in Fig. 2. To further elucidate this trend, we also show the corresponding Fermi surfaces as a function of pressure in the  $k_z = 0$  and  $k_z = 1/2$  planes in Fig. 3. While the size of the large hole-like  $\text{Ni-}d_{x^2-y^2}$  pocket does not change significantly with pressure or rare-earth size, the size of the electron pocket with  $R\text{-}d_{z^2}$  character around the  $\Gamma$ -point gradually increases with pressure (the  $R\text{-}d_{xy}$  pocket at the zone corners (A) remains essentially unchanged with pressure instead). While the effects on the  $R\text{-}5d$  pockets with hydrostatic and chemical pressure are similar, the latter systematically gives rise to a larger electron pocket at  $\Gamma$ . In any case, for both hydrostatic and chemical pressure the largest effect on the fermiology seems to be an increase in the amount of self-doping of the  $\text{Ni-}d_{x^2-y^2}$  band as the  $R\text{-}5d$  pockets become enlarged.

Moving to the changes in  $p-d$  hybridization, the complex of  $\text{O-}2p$  bands can be observed to shift down in energy with increasing pressure (both hydrostatic and chemical) while the  $\text{Ni-}3d$  states do not significantly move, consequently decreasing the degree of  $p-d$  hybridization (see Fig. 2). This is an unexpected effect that has been described before when analyzing the effects of chemical pressure in the infinite-layer nickelates [65, 66] (given that the lattice constants contract while the bandwidth increases one would in principle expect that the degree of covalency associated with the holes in the  $\text{Ni-O}$  planes should also increase). With these considerations, to obtain an estimate of the change in the degree of  $p-d$  hybridization with pressure, we calculate the charge-transfer energy evolution  $\Delta_{\text{CT}} = \varepsilon_d - \varepsilon_p$  (referring to  $d_{x^2-y^2}$  and  $p\sigma$ ) from the on-site energies of MLWFs (see relevant Wannier fits in Figs. 8 and 9 and on-site energies and hopping integrals in Table II in Appendix D). The derived values

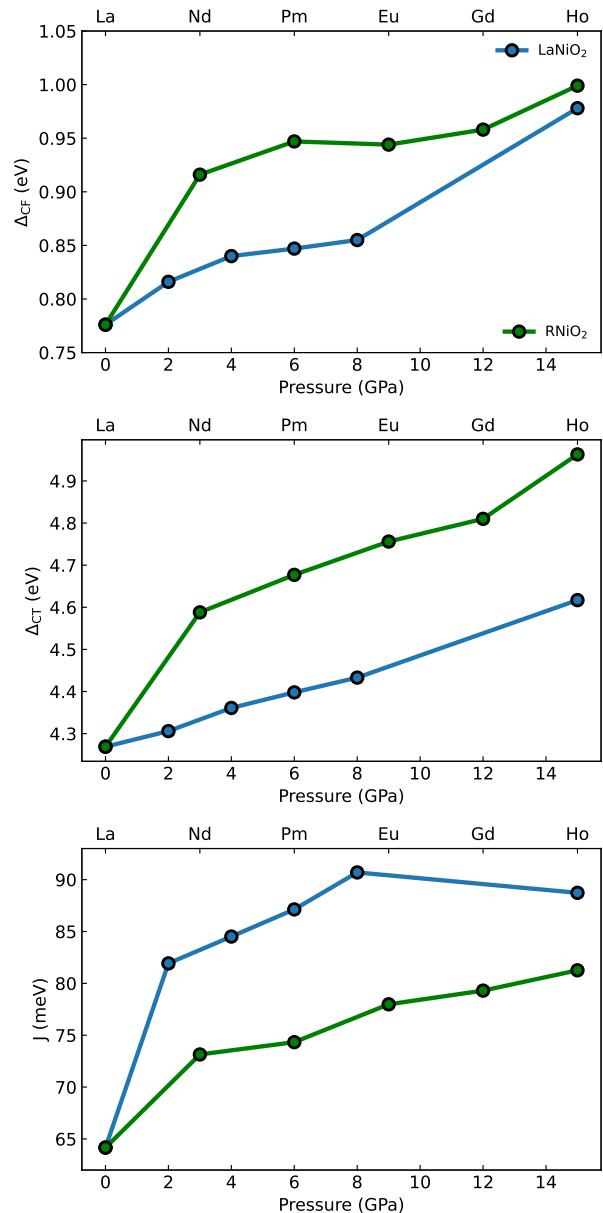


FIG. 4. Quantitative trends in the electronic structure of  $\text{RNiO}_2$  with hydrostatic and chemical pressure obtained from MLWFs (from top to bottom): crystal-field ( $\Delta_{\text{CF}}$ ) between the  $\text{Ni-}e_g$  orbitals, charge-transfer energy ( $\Delta_{\text{CT}}$ ) and estimated superexchange  $J$ .

of  $\Delta_{\text{CT}}$  with pressure are shown in Fig. 4 where  $\Delta_{\text{CT}}$  can be seen to increase from 4.27 eV at ambient pressure up to 4.62 eV at 15 GPa in  $\text{LaNiO}_2$ . A slightly larger increase is obtained when changing the rare-earth size, with  $\Delta_{\text{CT}}$  increasing from 4.59 eV to 4.96 eV when going from  $\text{NdNiO}_2$  to  $\text{HoNiO}_2$ .

Using the on-site energies from MLWFs (see Table II in Appendix D), we also analyze the evolution of the  $\text{Ni-}e_g$  crystal-field splitting defined as  $\Delta_{\text{CF}} = \varepsilon_{d_{x^2-y^2}} - \varepsilon_{d_{z^2}}$  that can be seen to systematically increase with both

hydrostatic and chemical pressure from  $\sim 0.78$  eV at ambient pressure for  $\text{LaNiO}_2$  to  $\sim 1$  eV for 15 GPa and  $\text{HoNiO}_2$  (see Figure 4). As mentioned above, a larger value of  $\Delta_{\text{CF}}$  in the cuprates is correlated with a higher  $T_c$  due to the reduced mixing of these orbitals [48, 49].

### C. Magnetic tendencies with pressure

In cuprates, the ground state of the undoped compounds (at nominal  $d^9$  filling) is an antiferromagnetic (AFM) charge-transfer insulator [2]. In infinite-layer nickelates the situation is slightly different: as mentioned above, there is evidence of short-range antiferromagnetic fluctuations from RIXS [56] even though long-range magnetic order has not been confirmed likely due to the interference of the R-5d bands. Regardless, within DFT (and DFT+ $U$ ) calculations, an antiferromagnetic ground state is obtained at ambient pressure [3, 50, 66]. Hence, to better understand the magnetic tendencies with pressure, we perform spin-polarized calculations and compare the energies of the two most stable magnetic states in  $\text{LaNiO}_2$  at ambient pressure (G-type AFM and C-type AFM). Fig. 5 shows the evolution of the energy difference between these two magnetic states with pressure (hydrostatic and chemical) at  $U = 2$  eV (results for  $U = 7$  eV are shown in Fig. 10 in Appendix E). For  $\text{LaNiO}_2$  the G-type AFM state is the ground state up to 15 GPa (and it is further stabilized as pressure is increased). For  $\text{RNiO}_2$ , as we move to the right in the lanthanide series, the G-AFM state continues being the ground state up to Gd, becoming less stable as chemical pressure is increased. Eventually, a crossover occurs, so that for Ho the magnetic ground state is C-type AFM. At  $U = 7$  eV, the G-type AFM state becomes even further stabilized as shown in Fig. 10 in Appendix E.

As mentioned above, in cuprates, there is a general consensus that magnetism is a key aspect underlying their physics, with the energy scale of  $T_c$  being set by the large values of the superexchange ( $J$ ). We will also use the scale of  $J$  here as a predictor of the superconducting tendencies in the infinite-layer nickelates with pressure. One can in principle extract estimates for the exchange constants from DFT-energy maps to a Heisenberg model. However, for  $\text{RNiO}_2$  the moments obtained in some of the magnetic solutions disproportionate, implying that such a mapping is not appropriate. Hence, to estimate the evolution of the magnetic superexchange, we resort to using both the Mott- and charge-transfer limits in the Zaanen-Sawatzky-Allen (ZSA) phase diagram [72] (given that in these materials  $U \sim \Delta_{\text{CT}}$ ),

$$J = \frac{2t_{pd}^4}{\Delta_{\text{CT}}^2} \times \left( \frac{1}{U_{dd}} + \frac{1}{\Delta_{\text{CT}} + \frac{1}{2}U_{pp}} \right)$$

Using our estimates for  $\Delta_{\text{CT}}$  and  $t_{pd}$  derived from the wannierizations, together with values of  $U_{pp} = 7.35$  eV and  $U_{dd} = 6.00$  eV characteristic of the cuprates [74] we

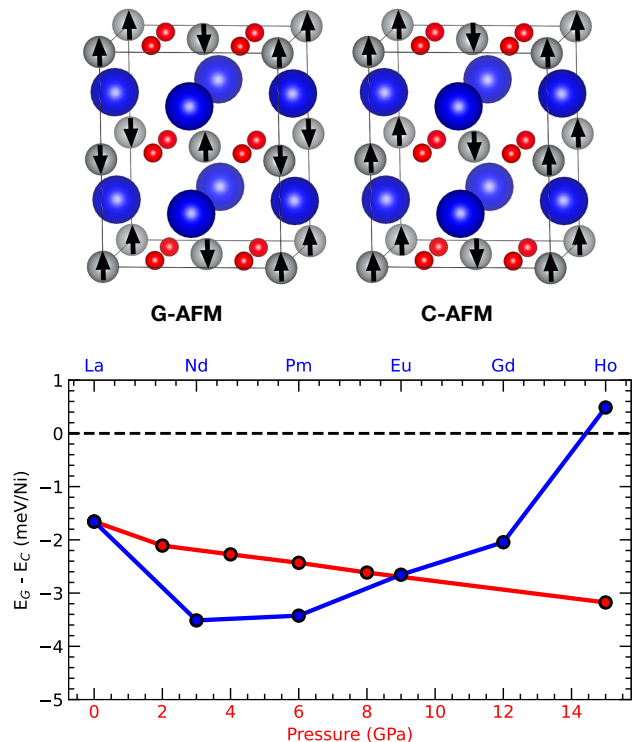


FIG. 5. Magnetic tendencies of  $\text{RNiO}_2$  with hydrostatic and chemical pressure. Top panel: AFM-G (left) and AFM-C (right) spin configurations. Bottom panel: Energy difference between the G-type and C-type antiferromagnetic states with hydrostatic and chemical pressure within GGA-PBE+ $U$  ( $U = 2$  eV) for  $\text{RNiO}_2$ . The curve in blue shows the energy difference for  $\text{LaNiO}_2$ , the red curve shows the same energy difference for  $\text{RNiO}_2$  (R= Nd, Pm, Eu, Gd, and Ho). The G-type AFM state is the ground state throughout except for Ho.

obtain a  $J$  value for  $\text{LaNiO}_2$  at ambient pressure  $\sim 65$  meV (very similar to the experimental value obtained from fittings of the spin wave dispersion derived from RIXS [56]). Importantly, we find that  $J$  increases to a cuprate-like value of  $\sim 90$  meV at a modest pressure of 8 GPa as shown in Fig. 4. This large increase in the superexchange value (together with the main electronic structure trends described above) agree well with previous theoretical calculations [75], that have predicted an increase in the superconducting  $T_c$  of the hole-doped Pr infinite-layer nickelate with pressure.

## IV. SUMMARY AND CONCLUSIONS

We have investigated the evolution of the electronic structure and magnetic trends in infinite layer nickelates ( $\text{RNiO}_2$ ) with pressure using first-principles calculations. Our findings suggest that there is a one-to-one correspondence between hydrostatic and chemical pressure in these materials. Overall, our results show that pressure (both hydrostatic and chemical) tends to (i) increase the

R-5d self-doping effect, (ii) increase the Ni- $d_{x^2-y^2}$  bandwidth, (iii) increase the  $e_g$  splittings, (iv) decrease the degree of  $p-d$  hybridization, and (v) increase the superexchange ( $J$ ). Using the energy scale of  $J$  as a predictor of superconducting tendencies, we anticipate that hydrostatic pressure and rare-earth substitution can indeed be a feasible means to further increase  $T_c$  in this family of

materials.

## ACKNOWLEDGMENTS

We acknowledge NSF Grant No. DMR-2045826 and the ASU Research Computing Center for HPC resources.

## Appendix A: Additional crystal data for RNiO<sub>2</sub>

Table I summarizes the DFT-optimized out-of-plane ( $c$ ) lattice constants for pressurized LaNiO<sub>2</sub> and the corresponding in-plane lattice-matched RNiO<sub>2</sub>.

	0 GPa	2 GPa	4 GPa	6 GPa	8 GPa	15 GPa
$c(\text{\AA})$	3.371	3.369	3.353	3.334	3.316	3.262
	La	Nd	Pm	Eu	Gd	Ho
$c(\text{\AA})$	3.371	3.302	3.263	3.206	3.177	3.110

TABLE I. Optimized  $c$  lattice constants under applied pressure for LaNiO<sub>2</sub> and for RNiO<sub>2</sub> with R = Nd, Pm, Eu, Gd, and Ho. All the lattice constants are provided in  $\text{\AA}$ .

## Appendix B: Dynamical instability of RNiO<sub>2</sub>

As mentioned in the main text, it has been shown previously [67, 68] that above a critical rare-earth ionic radius, the  $P4/mmm$  crystal structure becomes unstable in RNiO<sub>2</sub> with a lattice instability at A transforming the space group from  $P4/mmm$  to  $I4/mcm$  (see Fig. 6(a)). However, as mentioned above, for LaNiO<sub>2</sub> the  $P4/mmm$  structure is stable for all pressures considered here (see Fig. 1(b)). For smaller rare-earth ions, we take Ho as an example and reproduce the results of previous work [67, 68], where a lattice instability appears at A (see Fig. 6(b)). This unstable mode corresponds to the  $A_4^-$  irreducible representation of the  $P4/mmm$  space group and leads to a crystal structure ( $I4/mcm$ ) with rotated oxygens. The distorted  $I4/mcm$  structure is dynamically stable as shown in Fig. 6(b) evidenced by the lack of imaginary phonon modes. However, if one applies hydrostatic pressure to HoNiO<sub>2</sub> we note that this lattice instability can be quenched (see Fig. 6(b)).

## Appendix C: Additional DFT data for RNiO<sub>2</sub> with hydrostatic and chemical pressure in the nonmagnetic state

Figure 7 summarizes the non-magnetic electronic structure for LaNiO<sub>2</sub> at additional pressures, and the corresponding lattice-matched rare-earth cation. The same trends as those described in the main text can be observed.

## Appendix D: Wannierization of the DFT bands

To obtain a more quantitative analysis of the DFT electronic structure, we downfold the DFT Kohn-Sham bands onto a  $d-p$  basis of MLWFS. While this procedure does not result in a unique basis, we find that our downfolding provides a faithful representation of the DFT bands. We compare our DFT bands to the MLWFs-derived bands in Fig. 8 (for different pressures applied to LaNiO<sub>2</sub>) and Fig. 9 (for different rare-earths) where excellent agreement can be observed. Our MLWFs are well-localized and atomic-like as indicated by the real space visualization of the MLWFs corresponding to the Ni- $d_{x^2-y^2}$  and Ni- $d_{z^2}$  orbitals (see Fig. 8).

On-site energies and relevant hopping integrals obtained from the Wannier Hamiltonians for different hydrostatic pressures and rare-earth cations are summarized in Table II (all quantities in units of eV). Note that O- $p_{\sigma(\pi)}$  corresponds to the in-plane bonding (anti-bonding) with the Ni- $d_{x^2-y^2}$  orbital. The in-plane hopping is estimated from  $t_{pd}$  which is the hopping integral from the Ni- $d_{x^2-y^2}$  to the bonding O- $p_{\sigma}$  orbital. The effective  $t_{dd}$  hopping is given by  $t_{dd} = t_{pd}^2/\Delta_{CT}$ . From this data, we derive the charge-transfer energy, Ni- $e_g$  splitting, as well as estimate the superexchange  $J$  as discussed in the main text.

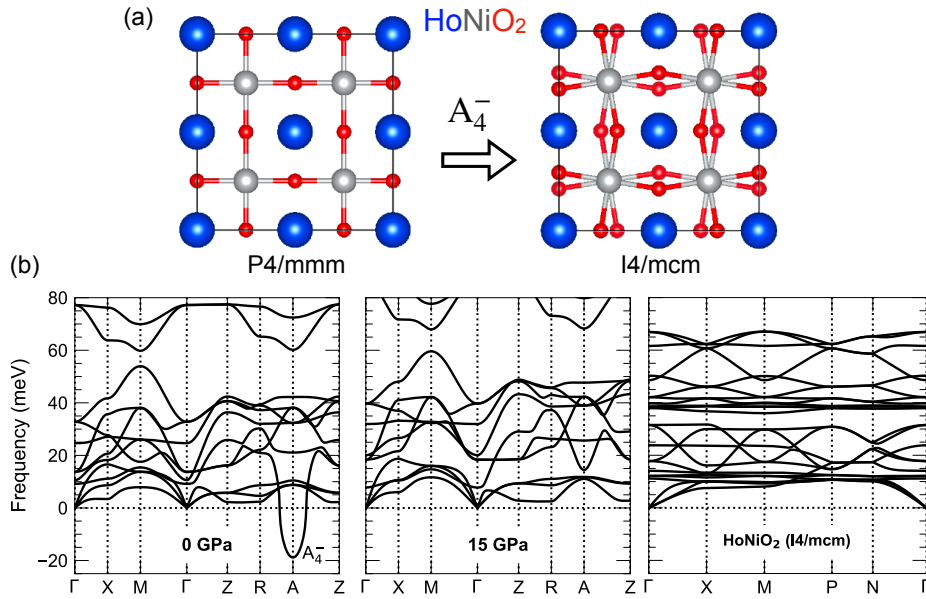


FIG. 6. Dynamical instability of  $\text{RNiO}_2$  infinite-layer nickelates. R = Ho is taken as an example. (a)  $\text{RNiO}_2$  crystal structure in the high-symmetry ( $P4/mmm$ ) phase (left) and low-symmetry, distorted phase ( $I4/mcm$ ) (right). (b) Phonon dispersions for  $\text{HoNiO}_2$  at ambient pressure (left) and 15 GPa (center) for the  $P4/mmm$  crystal structure. The soft-phonon mode at the A ( $\mathbf{q} = (1/2, 1/2, 1/2)$ ) point corresponds to an  $A_4^-$  normal mode. Phonon dispersion for  $\text{HoNiO}_2$  at ambient pressure in the  $I4/mcm$  space group with no imaginary phonon modes (right).

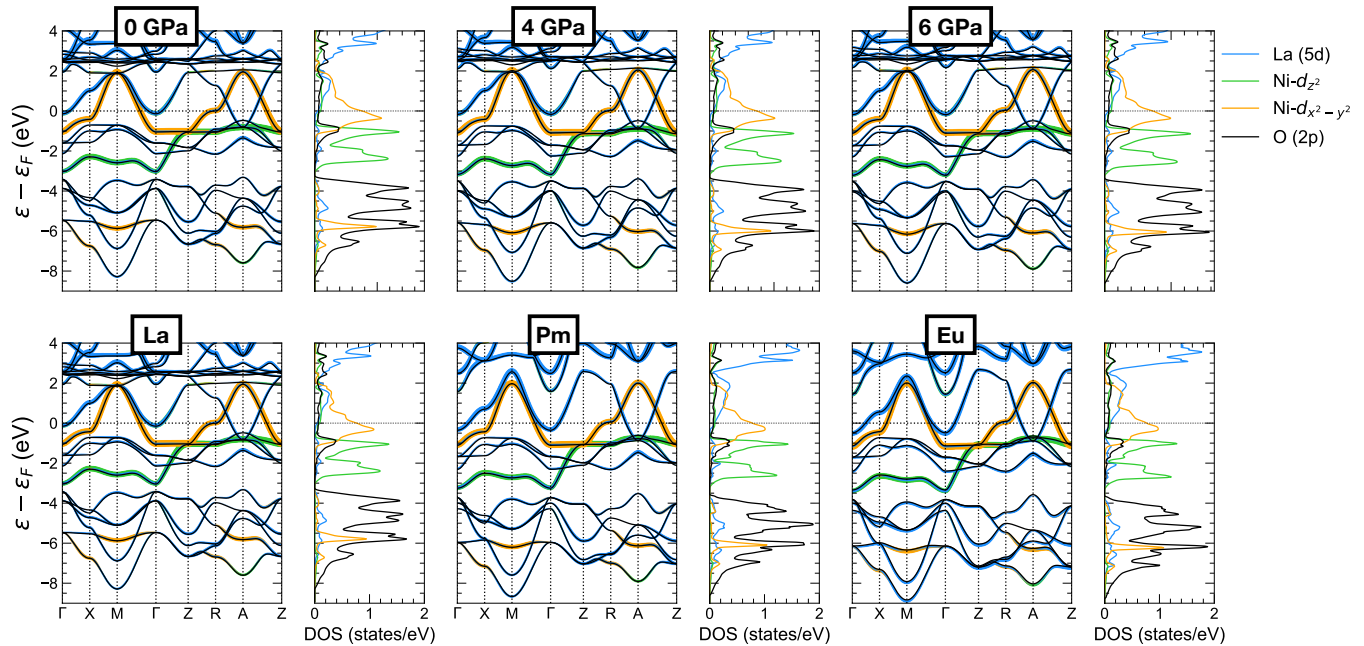


FIG. 7. Comparison between the non-magnetic electronic structure with hydrostatic (top) and chemical (bottom) pressure. Top row: Band structure along high-symmetry lines and atom-, orbital-resolved density of states (DOS) for  $\text{LaNiO}_2$  at ambient pressure, 4 GPa, and 6 GPa (from left to right). The orbital character of the bands is denoted for Ni- $d_{x^2-y^2}$  (orange), Ni- $d_{z^2}$  (green), and R- $d$  (blue). Bottom row: Equivalent plots as those of the top row for  $\text{RNiO}_2$  with R = La, Pm, and Eu (from left to right).

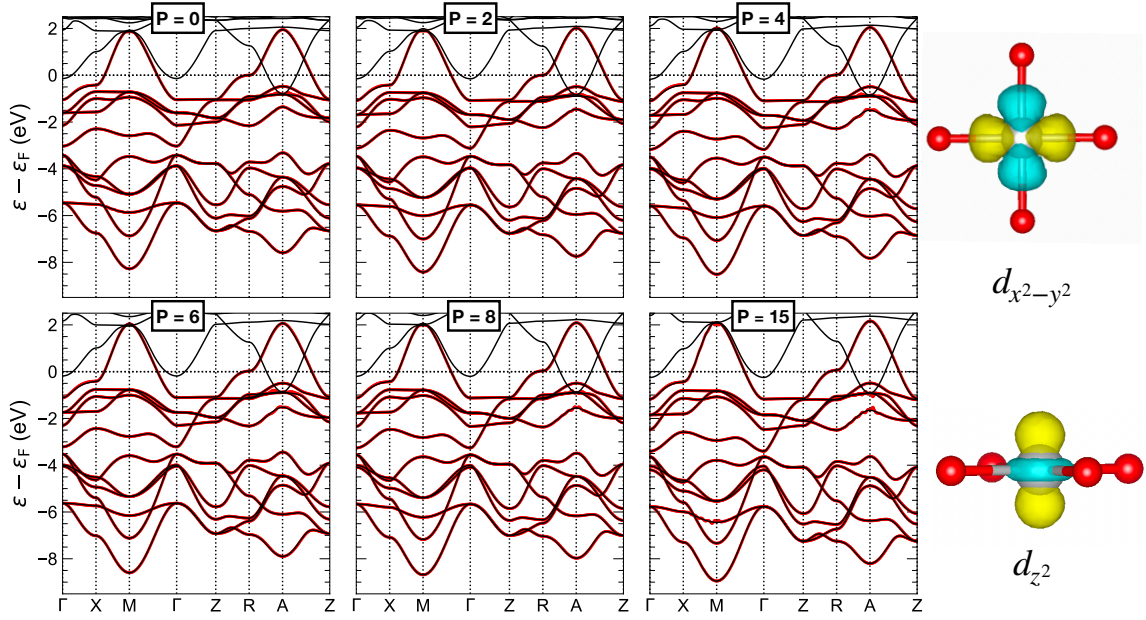


FIG. 8. Left panel: Comparison between the DFT bands (black) and the bands derived from our  $d-p$  MLWFs (red) for  $\text{LaNiO}_2$  for pressures up to 15 GPa. Right panel: Real-space visualization of the localized, atomic-like MLWFs corresponding to the  $\text{Ni-}e_g$  orbitals at ambient pressure.

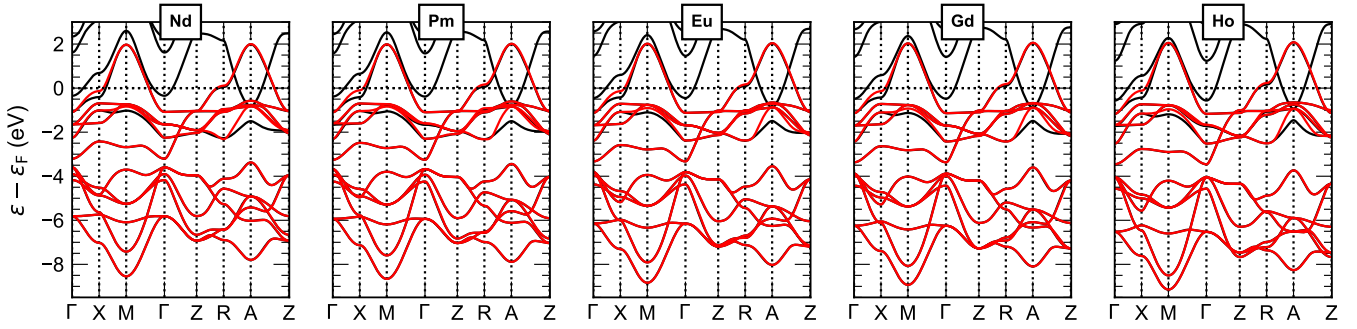


FIG. 9. Comparison between the DFT bands (black) and the bands derived from our  $d-p$  MLWFs (red) for  $\text{RNiO}_2$   $R = \text{Nd, Pm, Eu, Gd, and Ho}$ .

#### Appendix E: Additional DFT data for spin-polarized calculations in $\text{RNiO}_2$ with hydrostatic and chemical pressure

Fig. 10 shows the evolution with pressure of the energy difference between a C-type and a G-type AFM state at  $U = 7$  eV ( $J = 0.7$  eV). The G-type AFM state is more stable for all the pressures and rare-earth ions studied here. The energetics between AFM-C and AFM-G solutions vary throughout the literature (albeit the energy scales are rather small) indicating competition between aligning or anti-aligning the Ni moments out-of-plane [3, 65, 76].

	0 GPa	2 GPa	4 GPa	6 GPa	8 GPa	15 GPa
Wannier on-site energies (eV)						
Ni- $d_{x^2-y^2}$	-1.094	-1.138	-1.147	-1.163	-1.181	-1.172
Ni- $d_{z^2}$	-1.870	-1.954	-1.987	-2.010	-2.036	-2.150
Ni- $d_{xy}$	-1.748	-1.803	-1.840	-1.874	-1.911	-1.982
Ni- $d_{yz/xz}$	-1.632	-1.701	-1.733	-1.760	-1.787	-1.876
O- $p_\pi$	-4.485	-4.547	-4.589	-4.623	-4.659	-4.782
O- $p_\sigma$	-5.363	-5.444	-5.508	-5.561	-5.614	-5.789
O- $p_z$	-4.485	-4.567	-4.606	-4.639	-4.674	-4.764
Wannier hoppings (eV)						
Ni- $d_{x^2-y^2}$ -O- $p_\sigma$	-1.189	-1.270	-1.289	-1.305	-1.324	-1.347
Ni- $d_{z^2}$ - Ni- $d_{z^2}$ (001)	-0.365	-0.360	-0.367	-0.377	-0.386	-0.389
	NdNiO2	PmNiO2	EuNiO2	GdNiO2	HoNiO2	
Wannier on-site energies (eV)						
Ni- $d_{x^2-y^2}$	-0.998	-0.992	-1.037	-1.049	-1.058	
Ni- $d_{z^2}$	-1.914	-1.939	-1.981	-2.007	-2.057	
Ni- $d_{xy}$	-1.785	-1.813	-1.882	-1.914	-1.981	
Ni- $d_{yz/xz}$	-1.636	-1.660	-1.735	-1.767	-1.820	
O- $p_\pi$	-4.847	-4.964	-5.170	-5.271	-5.540	
O- $p_\sigma$	-5.586	-5.669	-5.793	-5.859	-6.021	
O- $p_z$	-4.810	-4.901	-5.064	-5.142	-5.342	
Wannier hoppings (eV)						
Ni- $d_{x^2-y^2}$ -O- $p_\sigma$	-1.279	-1.298	-1.326	-1.340	-1.372	
Ni- $d_{z^2}$ -Ni- $d_{z^2}$ (001)	-0.420	-0.436	-0.459	-0.469	-0.500	

TABLE II. Summary of calculated on-site energies and hopping integrals from Wannier functions for pressurized LaNiO<sub>2</sub> and RNiO<sub>2</sub> (R= Nd, Pm, Eu, Gd, Ho). O- $p_{\pi(\sigma)}$  denotes the anti-bonding (bonding) O- $p$  orbital in the NiO<sub>2</sub> plane. The effective  $dd$  hopping ( $t_{dd}$ ) is given by  $t_{dp}^2/\Delta_{CT}$ , where  $t_{dp}$  is  $d_{x^2-y^2} - p_\sigma$  and  $\Delta_{CT} = \varepsilon_{d_{x^2-y^2}} - \varepsilon_{p_\sigma}$ . All quantities are units of eV.

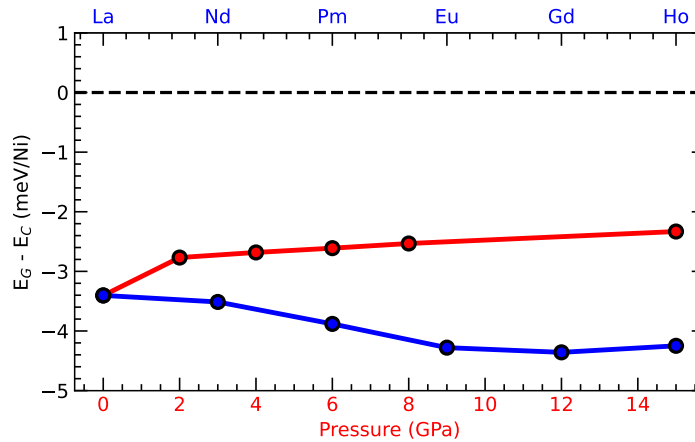


FIG. 10. Evolution of the energy difference between the G-type and C-type AFM states with hydrostatic and chemical pressure at  $U = 7$  eV ( $J = 0.68$  eV).

- 
- [1] J. G. Bednorz and K. A. Müller, *Z. Phys. B* **64**, 189 (1986).
- [2] B. Keimer, S. A. Kivelson, M. R. Norman, S. Uchida, and J. Zaanen, *Nature* **518**, 179 (2015).
- [3] K.-W. Lee and W. E. Pickett, *Phys. Rev. B* **70**, 165109 (2004).
- [4] V. I. Anisimov, D. Bukhvalov, and T. M. Rice, *Phys. Rev. B* **59**, 7901 (1999).
- [5] D. Li, K. Lee, B. Y. Wang, M. Osada, S. Crossley, H. R. Lee, Y. Cui, Y. Hikita, and H. Y. Hwang, *Nature* **572**, 624 (2019).
- [6] M. Osada, B. Y. Wang, B. H. Goodge, K. Lee, H. Yoon, K. Sakuma, D. Li, M. Miura, L. F. Kourkoutis, and H. Y. Hwang, *Nano Lett.* **20**, 5735 (2020).
- [7] M. Hepting, D. Li, C. J. Jia, H. Lu, E. Paris, Y. Tseng, X. Feng, M. Osada, E. Been, Y. Hikita, Y.-D. Chuang, Z. Hussain, K. J. Zhou, A. Nag, M. Garcia-Fernandez, M. Rossi, H. Y. Huang, D. J. Huang, Z. X. Shen, T. Schmitt, H. Y. Hwang, B. Moritz, J. Zaanen, T. P. Devereaux, and W. S. Lee, *Nat. Mater.* **19**, 381 (2020).
- [8] D. Li, B. Y. Wang, K. Lee, S. P. Harvey, M. Osada, B. H. Goodge, L. F. Kourkoutis, and H. Y. Hwang, *Phys. Rev. Lett.* **125**, 027001 (2020).
- [9] B.-X. Wang, H. Zheng, E. Kriviyakina, O. Chmaissem, P. P. Lopes, J. W. Lynn, L. C. Gallington, Y. Ren, S. Rosenkranz, J. F. Mitchell, and D. Phelan, *Phys. Rev. Mater.* **4**, 084409 (2020).
- [10] M. Osada, B. Y. Wang, B. H. Goodge, S. P. Harvey, K. Lee, D. Li, L. F. Kourkoutis, and H. Y. Hwang, *Adv. Mater.* **33**, 2104083 (2021).
- [11] X. Wu, D. Di Sante, T. Schwemmer, W. Hanke, H. Y. Hwang, S. Raghu, and R. Thomale, *Phys. Rev. B* **101**, 060504(R) (2020).
- [12] L.-H. Hu and C. Wu, *Phys. Rev. Res.* **1**, 032046(R) (2019).
- [13] P. Jiang, L. Si, Z. Liao, and Z. Zhong, *Phys. Rev. B* **100**, 201106(R) (2019).
- [14] M. Jiang, M. Berciu, and G. A. Sawatzky, *Phys. Rev. Lett.* **124**, 207004 (2020).
- [15] Y. Nomura, M. Hirayama, T. Tadano, Y. Yoshimoto, K. Nakamura, and R. Arita, *Phys. Rev. B* **100**, 205138 (2019).
- [16] M.-Y. Choi, K.-W. Lee, and W. E. Pickett, *Phys. Rev. B* **101**, 020503(R) (2020).
- [17] M.-Y. Choi, W. E. Pickett, and K.-W. Lee, *Phys. Rev. Res.* **2**, 033445 (2020).
- [18] S. Ryee, M. J. Han, and S. Choi, *Phys. Rev. Lett.* **126**, 206401 (2021).
- [19] S. Ryee, H. Yoon, T. J. Kim, M. Y. Jeong, and M. J. Han, *Phys. Rev. B* **101**, 064513 (2020).
- [20] Y. Gu, S. Zhu, X. Wang, J. Hu, and H. Chen, *Commun. Phys.* **3**, 84 (2020).
- [21] J. Karp, A. S. Botana, M. R. Norman, H. Park, M. Zingl, and A. Millis, *Phys. Rev. X* **10**, 021061 (2020).
- [22] J. Karp, A. Hampel, and A. J. Millis, *Phys. Rev. B* **103**, 195101 (2021).
- [23] I. Leonov, S. L. Skornyakov, and S. Y. Savrasov, *Phys. Rev. B* **101**, 241108(R) (2020).
- [24] F. Lechermann, *Phys. Rev. B* **101**, 081110(R) (2020).
- [25] F. Lechermann, *Phys. Rev. X* **10**, 041002 (2020).
- [26] H. Sakakibara, H. Usui, K. Suzuki, T. Kotani, H. Aoki, and K. Kuroki, *Phys. Rev. Lett.* **125**, 077003 (2020).
- [27] Y. Wang, C.-J. Kang, H. Miao, and G. Kotliar, *Phys. Rev. B* **102**, 161118(R) (2020).
- [28] F. Petocchi, V. Christiansson, F. Nilsson, F. Aryasetiawan, and P. Werner, *Phys. Rev. X* **10**, 041047 (2020).
- [29] P. Werner and S. Hoshino, *Phys. Rev. B* **101**, 041104(R) (2020).
- [30] Q. Gu, Y. Li, S. Wan, H. Li, W. Guo, H. Yang, Q. Li, X. Zhu, X. Pan, Y. Nie, and H.-H. Wen, *Nature Communications* **11**, 6027 (2020).
- [31] J. Krishna, H. LaBollita, A. O. Fumega, V. Pardo, and A. S. Botana, *Phys. Rev. B* **102**, 224506 (2020).
- [32] M. Kitatani, L. Si, O. Janson, R. Arita, Z. Zhong, and K. Held, *npj Quantum Mater.* **5**, 59 (2020).
- [33] C.-J. Kang and G. Kotliar, *Phys. Rev. Lett.* **126**, 127401 (2021).
- [34] K. Lee, B. H. Goodge, D. Li, M. Osada, B. Y. Wang, Y. Cui, L. F. Kourkoutis, and H. Y. Hwang, *APL Mater.* **8**, 041107 (2020).
- [35] Q. Li, C. He, J. Si, X. Zhu, Y. Zhang, and H.-H. Wen, *Commun. Mater.* **1**, 16 (2020).
- [36] B. H. Goodge, D. Li, K. Lee, M. Osada, B. Y. Wang, G. A. Sawatzky, H. Y. Hwang, and L. F. Kourkoutis, *Proc. Natl. Acad. Sci.* **118**, e2007683118 (2021).
- [37] M. Osada, B. Y. Wang, K. Lee, D. Li, and H. Y. Hwang, *Phys. Rev. Materials* **4**, 121801(R) (2020).
- [38] S. Zeng, C. Li, L. E. Chow, Y. Cao, Z. Zhang, C. S. Tang, X. Yin, Z. S. Lim, J. Hu, P. Yang, and A. Ariando, *Sci. Adv.* **8**, eabl9927 (2022).
- [39] G. A. Pan, D. Ferenc Segedin, H. LaBollita, Q. Song, E. M. Nica, B. H. Goodge, A. T. Pierce, S. Doyle, S. Novakov, D. Córdova Carrizales, A. T. N'Diaye, P. Shafer, H. Paik, J. T. Heron, J. A. Mason, A. Yacoby, L. F. Kourkoutis, O. Erten, C. M. Brooks, A. S. Botana, and J. A. Mundy, *Nat. Mater.* **21**, 160 (2022).
- [40] H. Sun, M. Huo, X. Hu, J. Li, Z. Liu, Y. Han, L. Tang, Z. Mao, P. Yang, B. Wang, J. Cheng, D.-X. Yao, G.-M. Zhang, and M. Wang, *Nature* **621**, 493 (2023).
- [41] J. Hou, P.-T. Yang, Z.-Y. Liu, J.-Y. Li, P.-F. Shan, L. Ma, G. Wang, N.-N. Wang, H.-Z. Guo, J.-P. Sun, Y. Uwatoko, M. Wang, G.-M. Zhang, B.-S. Wang, and J.-G. Cheng, *Chin. Phys. Lett.* **40**, 117302 (2023).
- [42] Y. Zhang, D. Su, Y. Huang, H. Sun, M. Huo, Z. Shan, K. Ye, Z. Yang, R. Li, M. Smidman, M. Wang, L. Jiao, and H. Yuan, *arXiv:2307.14819* (2023).
- [43] M. Zhang, C. Pei, X. Du, Y. Cao, Q. Wang, J. Wu, Y. Li, Y. Zhao, C. Li, W. Cao, S. Zhu, Q. Zhang, N. Yu, P. Cheng, J. Zhao, Y. Chen, H. Guo, L. Yang, and Y. Qi, *arXiv:2311.07423* (2023).
- [44] Q. Li, Y.-J. Zhang, Z.-N. Xiang, Y. Zhang, X. Zhu, and H.-H. Wen, *Chin. Phys. Lett.* **41**, 017401 (2024).
- [45] Y. Zhu, E. Zhang, B. Pan, X. Chen, D. Peng, L. Chen, H. Ren, F. Liu, N. Li, Z. Xing, J. Han, J. Wang, D. Jia, H. Wo, Y. Gu, Y. Gu, L. Ji, W. Wang, H. Gou, Y. Shen, T. Ying, X. Chen, W. Yang, C. Zheng, Q. Zeng, J.-G. Guo, and J. Zhao, *arXiv:2311.07353* (2024).
- [46] M. Crespin, P. Levitz, and L. Gatineau, *J. Chem. Soc., Faraday Trans. 2* **79**, 1181 (1983).
- [47] M. A. Hayward, M. A. Green, M. J. Rosseinsky, and J. Sloan, *J. Am. Chem. Soc.* **121**, 8843 (1999).
- [48] H. Sakakibara, H. Usui, K. Kuroki, R. Arita, and H. Aoki, *Phys. Rev. B* **85**, 064501 (2012).

- [49] H. Sakakibara, K. Suzuki, H. Usui, S. Miyao, I. Maruyama, K. Kusakabe, R. Arita, H. Aoki, and K. Kuroki, *Phys. Rev. B* **89**, 224505 (2014).
- [50] A. S. Botana and M. R. Norman, *Phys. Rev. X* **10**, 011024 (2020).
- [51] B. Cheng, D. Cheng, K. Lee, L. Luo, Z. Chen, Y. Lee, B. Y. Wang, M. Mootz, I. E. Perakis, Z.-X. Shen, H. Y. Hwang, and J. Wang, *Nature Materials* (2024), 10.1038/s41563-023-01766-z.
- [52] S. P. Harvey, B. Y. Wang, J. Fowlie, M. Osada, K. Lee, Y. Lee, D. Li, and H. Y. Hwang, *arXiv:2201.12971* (2022).
- [53] N. N. Wang, M. W. Yang, Z. Yang, K. Y. Chen, H. Zhang, Q. H. Zhang, Z. H. Zhu, Y. Uwatoko, L. Gu, X. L. Dong, J. P. Sun, K. J. Jin, and J.-G. Cheng, *Nature Communications* **13**, 4367 (2022).
- [54] L. Gao, Y. Y. Xue, F. Chen, Q. Xiong, R. L. Meng, D. Ramirez, C. W. Chu, J. H. Eggert, and H. K. Mao, *Phys. Rev. B* **50**, 4260 (1994).
- [55] A. S. Botana, K.-W. Lee, M. R. Norman, V. Pardo, and W. E. Pickett, *Frontiers in Physics* **9** (2022).
- [56] H. Lu, M. Rossi, A. Nag, M. Osada, D. F. Li, K. Lee, B. Y. Wang, M. Garcia-Fernandez, S. Agrestini, Z. X. Shen, E. M. Been, B. Moritz, T. P. Devereaux, J. Zaanen, H. Y. Hwang, K.-J. Zhou, and W. S. Lee, *Science* **373**, 213 (2021).
- [57] G. Kresse and J. Hafner, *Phys. Rev. B* **48**, 13115 (1993).
- [58] G. Kresse and J. Furthmüller, *Computational Materials Science* **6**, 15 (1996).
- [59] J. P. Perdew, K. Burke, and M. Ernzerhof, *Phys. Rev. Lett.* **77**, 3865 (1996).
- [60] A. Togo and I. Tanaka, *Scripta Materialia* **108**, 1 (2015).
- [61] P. Blaha, K. Schwarz, F. Tran, R. Laskowski, G. K. H. Madsen, and L. D. Marks, *J. Chem. Phys.* **152**, 074101 (2020).
- [62] A. A. Mostofi, J. R. Yates, G. Pizzi, Y.-S. Lee, I. Souza, D. Vanderbilt, and N. Marzari, *Comput. Phys. Commun.* **185**, 2309 (2014).
- [63] J. Kunes, R. Arita, P. Wissgott, A. Toschi, H. Ikeda, and K. Held, *Comput. Phys. Commun.* **181**, 1888 (2010).
- [64] V. I. Anisimov, I. V. Solovyev, M. A. Korotin, M. T. Czyżyk, and G. A. Sawatzky, *Phys. Rev. B* **48**, 16929 (1993).
- [65] J. Kapeghian and A. S. Botana, *Phys. Rev. B* **102**, 205130 (2020).
- [66] E. Been, W.-S. Lee, H. Y. Hwang, Y. Cui, J. Zaanen, T. Devereaux, B. Moritz, and C. Jia, *Phys. Rev. X* **11**, 011050 (2021).
- [67] C. Xia, J. Wu, Y. Chen, and H. Chen, *Phys. Rev. B* **105**, 115134 (2022).
- [68] F. Bernardini, A. Bosin, and A. Cano, *Phys. Rev. Mater.* **6**, 044807 (2022).
- [69] M.-C. Jung, H. LaBollita, V. Pardo, and A. S. Botana, *Scientific Reports* **12**, 17864 (2022).
- [70] H. LaBollita, A. Hampel, J. Karp, A. S. Botana, and A. J. Millis, *Phys. Rev. B* **107**, 205155 (2023).
- [71] C. Weber, C. Yee, K. Haule, and G. Kotliar, *Europhysics Letters* **100**, 37001 (2012).
- [72] J. Zaanen, G. A. Sawatzky, and J. W. Allen, *Phys. Rev. Lett.* **55**, 418 (1985).
- [73] Y. Shen, J. Sears, G. Fabbris, J. Li, J. Pellicciari, I. Jarrige, X. He, I. Božović, M. Mitran, J. Zhang, J. F. Mitchell, A. S. Botana, V. Bisogni, M. R. Norman, S. Johnston, and M. P. M. Dean, *Phys. Rev. X* **12**, 011055 (2022).
- [74] A. K. McMahan, R. M. Martin, and S. Satpathy, *Phys. Rev. B* **38**, 6650 (1988).
- [75] S. D. Cataldo, P. Worm, J. Tomczak, L. Si, and K. Held, *arXiv:2311.06195* (2023).
- [76] Z. Liu, Z. Ren, W. Zhu, Z. Wang, and J. Yang, *npj Quantum Mater.* **5**, 31 (2020).